*Battery Energy*

WILEY

RESEARCH ARTICLE OPEN ACCESS

# Tailoring MXene/Nickel Cobalt Phosphate Composite for Enhanced Electrochromic and Supercapacitor Applications

Muhammad Norhaffis Mustafa[1] | Muhammad Amirul Aizat Mohd Abdah[2] | Norshahirah Mohamad Saidi[3] | Arshid Numan[1,4] | Yusran Sulaiman[5,6] | Rashmi Walvekar[7,8] | Mohammad Khalid[9,10,11]

[1]Sunway Centre for Electrochemical Energy and Sustainable Technology (SCEEST), Faculty of Engineering and Technology, Sunway University, No. 5, Jalan Universiti, Bandar Sunway, Darul Ehsan, Selangor, Malaysia | [2]Department of Chemistry, Faculty of Science, Universiti Teknologi Malaysia, Johor Bahru, Johor, Malaysia | [3]Department of Physics, Faculty of Science, Universiti Teknologi Malaysia, Skudai, Johor, Malaysia | [4]Department of Applied Physics, Saveetha School of Engineering, Saveetha University (SIMATS), Chennai, India | [5]Department of Chemistry, Faculty of Science, Universiti Putra Malaysia, UPM, Serdang, Selangor, Malaysia | [6]Functional Nanotechnology Devices Laboratory, Institute of Nanoscience and Nanotechnology (ION2), Universiti Putra Malaysia, Serdang, Selangor, Malaysia | [7]Department of Chemical and Process Engineering, University of Strathclyde, Glasgow, UK | [8]Centre for Research Impact and Outcome, Chitkara University, Rajpura, Punjab, India | [9]Materials and Manufacturing Research Group, James Watt School of Engineering, University of Glasgow, UK | [10]Faculty of Engineering, Manipal University Jaipur, Rajasthan, India | [11]University Centre for Research and Development, Chandigarh University, Mohali, Punjab, India

**Correspondence:** Arshid Numan (numan.arshed@yahoo.com) | Mohammad Khalid (mohammad.khalid@glasgow.ac.uk)

**Received:** 20 September 2025 | **Revised:** 22 November 2025 | **Accepted:** 25 November 2025

**Keywords:** coloration efficiency | composite electrode | electrochromic | energy storage | MXene | nickel cobalt phosphate | supercapacitor

## ABSTRACT

Electrochromic materials that simultaneously enable optical modulation and charge storage offer a promising route toward multifunctional energy systems. Herein, we report a scalable synthesis of a nickel cobalt phosphate–MXene (NCP/$Ti_3C_2$) composite engineered to couple fast ion transport with structural robustness. Using microwave-assisted deposition followed by spin coating, we constructed a conductive $Ti_3C_2$ network that intimately overlays the NCP matrix, forming an architecture that overcomes the transport limitations and instability typically observed in MXene–phosphate hybrids. The optimized NCP/$Ti_3C_2$ film delivered a high coloration efficiency (~140 $cm^2$/C) and retained over 75% of its optical contrast after 1000 switching cycles. It further exhibits an exceptional specific capacitance (~2300 F/g at 1 mV/s), reflecting markedly enhanced charge-storage kinetics. Assembled into an asymmetric electrochromic supercapacitor with activated carbon, the device achieved an energy density of ~15 Wh/kg at a power density of ~1600 W/kg and maintained ~85% capacitance retention over 5000 cycles. These combined optical and electrochemical performances position the NCP/$Ti_3C_2$//AC system as a compelling platform for next-generation wearable and multifunctional energy-storage technologies.

## 1 | Introduction

The growing demand for electric and hybrid electric cars and electronic gadgets has prompted researchers to focus on the development of energy storage devices with multifunctional, high energy and power densities, and extended lifespans. Increased environmental concerns have spurred the use of natural energy sources, such as wind [1, 2], solar [3–5], and hydropower [6, 7]. However, the intermittent nature of these resources highlights the urgent need for efficient energy storage and conversion technologies that can meet rising global energy demands [8, 9]. Electrochromic energy storage devices (EESDs), a subclass of multifunctional supercapacitors, have emerged as promising candidates because they not only enhance energy storage efficiency but

also provide esthetic and functional value, particularly in modern architecture [10–13]. When integrated into building façades, such as glass skyscrapers, EESDs offer dual advantages: they improve the visual appeal through voltage-induced color modulation, while simultaneously contributing to energy efficiency by storing excess energy for auxiliary applications, such as lighting [11, 13]. Despite these advantages, the practical deployment of EESDs remains limited, primarily because of their modest energy storage performance and poor cycling stability. These limitations stem from the redox-driven charge storage mechanism, which involves continuous ion insertion and extraction processes that accelerate material degradation [11, 13].

To address these challenges, the design of composite materials with synergistic properties has been proposed as a route for improving both their performance and durability. Bimetallic phosphates (BMPs) are particularly attractive because of their open-framework microporous structures, which are composed of tetrahedral $PO_4^{3-}$ anions and bimetallic cations, providing a large surface area and multiple ion migration channels for enhanced electrochemical activity [14–16]. However, their intrinsic pore size ($\leq 2$ nm) restricts electrolyte ion diffusion, limiting their rate capability [17]. To overcome these limitations, integrating BMPs with highly conductive $Ti_3C_2$ MXene is a promising strategy, as MXene offers a large surface area, excellent electrical conductivity, and efficient ion transport pathways [13, 18, 19]. This synergistic combination facilitates rapid electron/ion transfer and enhances structural stability, thereby enabling the design of high-performance hybrid electrodes. Among MXenes, $Ti_3C_2$ is particularly attractive for hybridization because of its hydrophilic surface chemistry and compatibility with spin-coating deposition techniques [13, 18, 19].

In this study, nickel cobalt phosphate (NCP) was integrated with $Ti_3C_2$ MXene through a rapid microwave-assisted synthesis and a sequential spin-coating technique. Optimization using response surface methodology and central composite design (RSM/CCD) allowed for precise control of the composition and structure. Compared with previously reported NCP/MXene-based electrodes, the present work demonstrates an enhanced specific capacitance (2270 F/g at 1 mV/s), higher coloration efficiency (132.68 $cm^2$/C), and superior optical contrast retention (75% over 1000 cycles), highlighting the novelty of the optimized NCP/$Ti_3C_2$ architecture and its potential for next-generation EESDs.

## 2 | Experimental

### 2.1 | Materials

Titanium aluminum carbide ($Ti_3AlC_2$, 400 mesh, 99.9%) was obtained from Xiamen TOB New Energy Technology Co. Ltd. (Xiamen, China). Sodium phosphate dibasic ($Na_2HPO_4$) and lithium hydroxide (LiOH) were purchased from Merck KGaA and Alfa Aesar, respectively. Cobaltous chloride hexahydrate ($CoCl_2{\cdot}6H_2O$) and activated carbon (AC) were supplied by Across, while hydrochloric acid (HCl, 37%), lithium fluoride (LiF), and fluorine-doped tin oxide (FTO)-coated glass substrates were procured from Sigma-Aldrich. Nickelous chloride hexahydrate ($NiCl_2{\cdot}6H_2O$), ethanol, and acetone were obtained from Fisher Scientific. Deionized water was used throughout all stages of electrode material preparation and device fabrication. All chemicals were used as received without further purification.

### 2.2 | Synthesis and Modification of NCP/$Ti_3C_2$ Electrode

The NCP/$Ti_3C_2$ electrode was synthesized and optimized using Design Expert software (version 12). RSM/CCD was employed to optimize the NCP/$Ti_3C_2$ electrode fabrication. Specifically, the optimization process focused on two key parameters: the concentration of NCP and $Ti_3C_2$, with the specific capacitance serving as the sole surface response variable. The detailed ranges of the parameters are listed in Table 1.

Microwave-assisted synthesis was adopted to rapidly produce high-purity NCP and $Ti_3C_2$ powders under mild conditions. NCP was prepared by mixing 0.1 M $NiCl_2{\cdot}6H_2O$, 0.1 M $CoCl_2{\cdot}6H_2O$, and 0.2 M $Na_2HPO_4$ in a Teflon vessel with stirring for 30 min, followed by microwave treatment at 124°C (4°C/min) for 10.5 min. The resulting powder was dried at 80°C for 12 h. Nickel phosphate (NP) and cobalt phosphate (CP) were synthesized in a similar manner, omitting the cobalt or nickel precursor, respectively.

$Ti_3C_2$ MXene was produced by selectively etching the Al component from $Ti_3AlC_2$ MAX phase using a 2.5 M LiF and 6 M HCl solution. $Ti_3AlC_2$ (0.5 g) was gradually added under constant stirring and sonicated for 30 min, and then subjected to microwave treatment at 40°C (1.5°C/min) for 40 min. The etched $Ti_3C_2$ was washed repeatedly with deionized water via centrifugation at 10,000 rpm until a neutral pH was achieved, followed by 60 min of ultrasonic exfoliation under an inert atmosphere. The exfoliated $Ti_3C_2$ sheets were recovered by centrifugation (10,000 rpm, 10 min) and freeze-dried to yield $Ti_3C_2$ powder.

The NCP/$Ti_3C_2$ electrode was fabricated using a sequential spin coating process. Based on the experimental design outlined in Table 1, solutions of NCP and $Ti_3C_2$ were prepared at 100 mg/mL in ethanol. First, 0.2 mL of the NCP solution (20–180 mg/mL in ethanol) was spin-coated onto a conductive glass substrate (1500 rpm, 30 s) and dried at 60°C for 1 h. Subsequently, 0.2 mL of $Ti_3C_2$ dispersion (1–3 mg/mL in ethanol) was applied to form the hybrid NCP/$Ti_3C_2$ electrode, followed

**TABLE 1** | List of independent parameters, notation, unit, actual, and coded level of the respective independent parameters.

| Parameters | Notation | Unit | Actual | | | Coded level | | |
|---|---|---|---|---|---|---|---|---|
| | | | Low | Middle | High | Low | Middle | High |
| Concentration of $Ti_3C_2$ | A | mg/mL | 1 | 2 | 3 | −1 | 0 | 1 |
| Concentration of NCP | B | mg/mL | 20 | 100 | 180 | −1 | 0 | 1 |

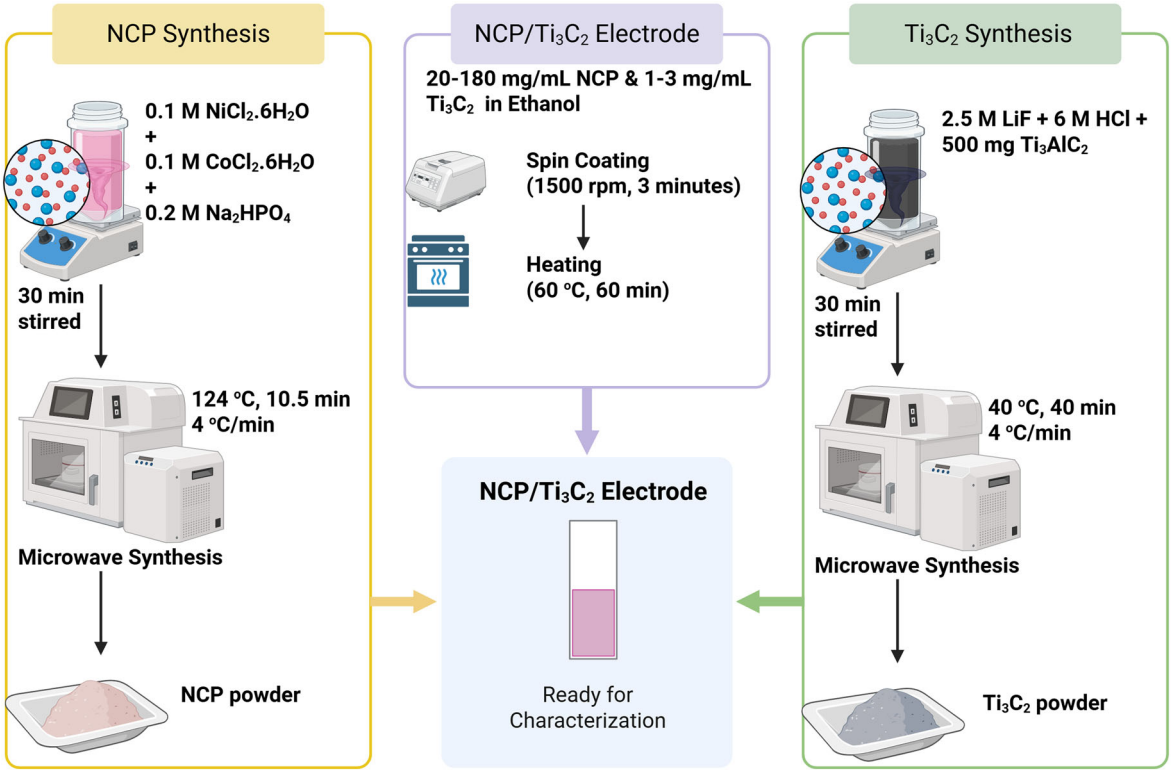


**FIGURE 1** | Schematic detailing the synthesis procedure of NCP/$Ti_3C_2$.

by oven drying at 70°C for 2 h. The resulting electrode exhibited a mass loading of 0.37 mg/cm$^2$ in a three-electrode system (3ES). A schematic diagram illustrating the synthesis procedure of NCP/$Ti_3C_2$ is presented in Figure 1. This microwave-assisted spin-coating strategy establishes a continuous, conductive $Ti_3C_2$ network over the NCP layer, promoting intimate interfacial contact and efficient electron/ion transport. The $Ti_3C_2$ overlayer not only enhances electrical conductivity but also mechanically stabilizes the NCP during repeated charge–discharge cycles. Compared with previously reported MXene-phosphate or binary metal phosphate electrodes, the optimized NCP/$Ti_3C_2$ composite delivered a superior specific capacitance and cycling stability, highlighting the synergistic interplay between the redox-active NCP and the conductive $Ti_3C_2$ scaffold.

## 2.3 | Material Characterization

The morphology of NCP/$Ti_3C_2$ was analyzed using field emission scanning microscopy (FESEM JEOL:JSM7800F) and high-resolution transmission electron microscopy (HRTEM, Zeiss Libra 200FE). The confirmation analysis of NCP/$Ti_3C_2$ was performed using Fourier-transform infrared spectroscopy (FTIR, Perkin Elmer Spectrum 1000), Raman spectroscopy (WITec GmbH, 532 nm), X-ray diffraction analysis (XRD, Shimadzu with Cu K radiation, $\lambda = 1.54$), and X-ray photoelectron spectroscopy (XPS, Thermo Scientific K-alpha).

## 2.4 | Electrochemical Measurements

The electrochemical experiments were systematically categorized into electrochromic and supercapacitive analyses. For electrochromic characterization, a 3ES was employed, with the NCP/$Ti_3C_2$ composite functioning as the working electrode, a saturated calomel electrode as the reference, and a platinum wire as the counter electrode. The supercapacitive behavior was assessed using both three- and two-electrode setups. In the two-electrode system (2ES), the NCP/NCP/$Ti_3C_2$ composite and AC served as the positive and negative electrodes, respectively, separated by filter paper immersed in 1 M LiOH electrolyte, which was consistent across all configurations. The electrochromic properties of the NCP/NCP/$Ti_3C_2$ composites were examined using an Autolab spectrophotometer. The key evaluated parameters included CE, $\Delta T$, bleaching time ($t_b$), and coloration time ($t_c$). $\Delta T$ quantifies the transmittance difference between bleached and colored states, while $t_b$ and $t_c$ denote the durations required to reach 95% of $\Delta T$ during bleaching and coloring, respectively. The coloration efficiency was determined using Equation (1):

$$\mathrm{CE} = \frac{\Delta(\mathrm{OD})}{Q_d} = \frac{A_b - A_c}{Q_d}, \quad (1)$$

where $A_{b/c}$, $Q_d$, and OD denote the absorbance in the bleached/colored state, charge density, and optical density, respectively. The durability of the NCP/$Ti_3C_2$ electrode was evaluated over 1000 switching cycles at a wavelength of 671 nm. Electrochemical characterization was performed on a VIONIC workstation equipped with INTELLO software, enabling cyclic voltammetry (CV), galvanostatic charge–discharge (GCD), and electrochemical impedance spectroscopy (EIS). CV and GCD measurements were conducted across a range of scan rates and current densities to probe the electrolyte response and charge storage behavior of the NCP/$Ti_3C_2$ hybrid. EIS spectra were

acquired from 100 kHz to 1 Hz using a 10 mV AC perturbation to extract resistive components associated with the active material. The specific capacitance, power density, and energy density were calculated using Equations (2–5).

$$Q_s = \frac{\int IdV}{mv}. \tag{2}$$

$$Q_s = \frac{I\Delta t}{m}, \tag{3}$$

$$P = \frac{E \times 3600}{\Delta t}, \tag{4}$$

$$E = \frac{Q_s \times \Delta V}{2 \times 3.6}, \tag{5}$$

where $\int IdV, v, m, I, \Delta t, P, \Delta V$ and $E$ represents the integrated area under the CV curves, scan rate (V/s), mass of active material (g), current (A), discharge time (s), power density (W/kg), operating voltage (V), and energy density (Wh/kg), respectively. The long-term electrochemical stability of the NCP/$Ti_3C_2$ electrode was evaluated using a Neware Battery Tester (BTS4000-5V10 mA) over 5000 continuous charge–discharge cycles.

## 3 | Results and Discussion

### 3.1 | Physical Studies

XRD analysis was performed to study the phase compositions of the electrode materials. Figure 2a shows the XRD patterns of NP, CP, $Ti_3C_2$, NCP, and NCP/$Ti_3C_2$. The NP exhibited XRD patterns at 20.8° (001), 33.42° (031), 35.44° (210), 38.58° (004), 40.78° (140), and 44.11° (14-1), which were assigned to the crystal structure of NP monoclinic (JCPDS No. 00-033-0950) [10, 12]. The CP demonstrated XRD patterns at 10.72° (110), 13.32° (020), 18.62° (011), 24.89° (11-1), 28.24° (111), 30.78° (10-2), 37.66° (102), 41.12° (21-1), 46.06° (20-2), 47.74° (211), 51.96° (113) and 55.6° (051), which are attributed to the monoclinic crystal system of CP (JCPDS No. 01-082-0521) [10, 12]. In contrast, $Ti_3C_2$ exhibited XRD patterns at 6.54° (002), 19.90° (004), 28.34° (006), 35.21° (008), 38.8° (104) and 60.71° (110), which belong to the $Ti_3C_2$ MXene in its crystalline form (JCPDS No. 00-032-1383) [10, 20–22]. The XRD pattern of NCP exhibits a combination of NP- and CP-type reflections, confirming the successful formation of the mixed-phase material. In the optimized NCP/$Ti_3C_2$ composite, the diffraction pattern retained the characteristic reflections of both NCP and $Ti_3C_2$; however, several low-intensity NCP peaks were noticeably weakened or indistinct. This attenuation likely arises from the homogeneous dispersion of NCP nanoparticles across the $Ti_3C_2$ surface, overlap between weak NCP reflections and more intense $Ti_3C_2$ peaks, and partial peak broadening induced by microwave-assisted synthesis. Such suppression and broadening effects are well documented in MXene-based hybrid systems [23, 24] and typically indicate strong interfacial coupling rather than the absence of a constituent phase. Complementary XPS analysis (Figure 2d–k) further corroborated the successful microwave-assisted formation of the NCP/$Ti_3C_2$ composite. The crystallite dimensions were estimated using the Scherrer equation. For the dominant NCP/$Ti_3C_2$ peak at $2\theta = 10.72°$ (110), the crystallite size was calculated to be 111.73 nm, whereas the peak at $2\theta = 13.32°$ (020) yielded a size of 145.11 nm. Crystallites exceeding ~50 nm are generally classified as large, suggesting a more ordered lattice with reduced defect density, which is often associated with improved electrical conductivity in mixed-phase composites [25].

FTIR analysis (Figure 2b) was conducted to identify the functional groups in electrode materials [26]. The FTIR spectrum of NP shows characteristic peaks at 578 and 1020 $cm^{-1}$, which correspond to the Ni—OH bending vibration and stretching vibration of P—O, respectively [27]. The FTIR spectrum of CP shows distinctive peaks at 863 and 1020 $cm^{-1}$, which are attributed to the vibration modes of Co—O and the stretching vibration of P—O, respectively [28]. In contrast, the FTIR spectrum of $Ti_3C_2$ shows two prominent peaks at 1641 and 524 $cm^{-1}$, which correspond to C═O and Ti—O, respectively [29]. Overall, the FTIR spectra of NCP and NCP/$Ti_3C_2$ exhibited all the characteristic peaks of the individual composites. Additionally, the broad peak at approximately 3443 $cm^{-1}$ is ascribed to the O—H stretching vibration [30, 31]. Compared with the pristine NCP and $Ti_3C_2$, several FTIR peaks of the NCP/$Ti_3C_2$ composite exhibited slight shifts in wavenumber and variations in intensity. These spectral changes can be attributed to interfacial interactions between the surface functional groups of $Ti_3C_2$ (—OH, —F, —O) and the metal–oxygen/phosphate bonds (Ni—O, Co—O, and P—O) of NCP [32, 33]. Such interactions lead to changes in bond polarity and local electronic environments, resulting in peak shifts. Partial charge transfer and lattice strain introduced during the microwave-assisted synthesis further contribute to these vibrational modifications [34]. Therefore, the FTIR peak shifts provide evidence of strong chemical coupling and successful hybridization between NCP and $Ti_3C_2$.

Raman spectroscopy (Figure 2c) was employed to probe the vibrational modes of the NCP/$Ti_3C_2$ electrode. The spectrum reveals distinct peaks at 151, 500, and 632 $cm^{-1}$, corresponding to TiC vibrations, confirming the presence of $Ti_3C_2$ MXene [35, 36]. Furthermore, the as-prepared NCP/$Ti_3C_2$ electrode exhibited characteristic peaks at 1337 and 1525 $cm^{-1}$, representing the D and G bands of graphitic carbon, respectively [35, 36]. The peak near 500 $cm^{-1}$ is attributed to Ni—O/Co—O stretching, whereas the feature around 1000 $cm^{-1}$ arises from P—O vibrations [37, 38]. Notably, several Raman bands of NCP/$Ti_3C_2$ show slight shifts and broadening relative to pristine NCP and $Ti_3C_2$, indicative of interfacial coupling and charge transfer between $Ti_3C_2$ layers and NCP species, which modify local bond force constants and vibrational frequencies [34, 39]. These spectral modifications corroborate strong electronic and structural interactions at the NCP/$Ti_3C_2$ interface, consistent with FTIR analysis and confirming the successful integration of the two components.

XPS was employed to elucidate the chemical states and surface composition of the optimized NCP/$Ti_3C_2$ electrode (Figure 2d–k). The survey spectrum confirms the presence of P, C, Ti, O, F, Co, and Ni, consistent with the incorporation of NCP species on the MXene scaffold (Figure 2d). The O1s region

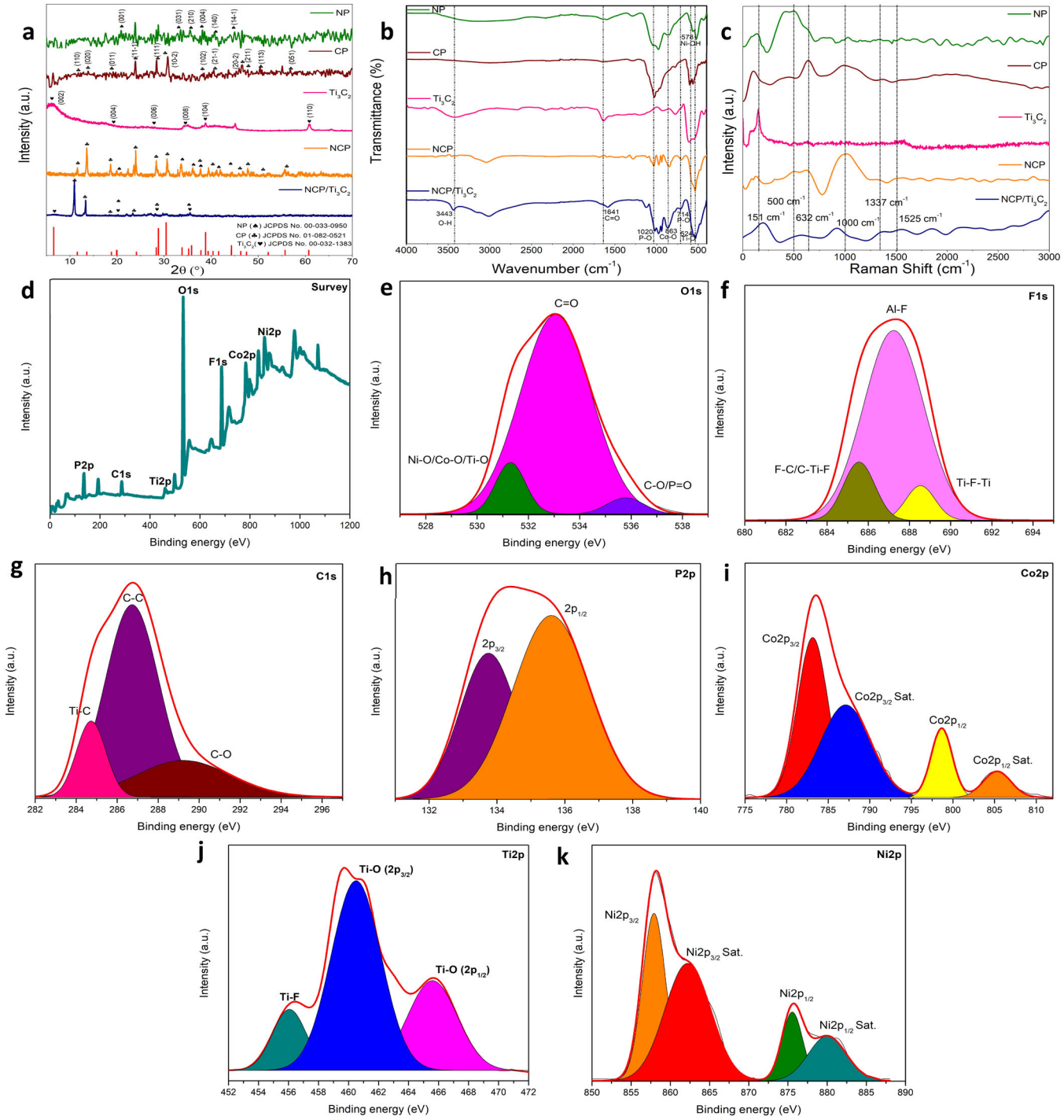


**FIGURE 2** | (a) XRD patterns of NP, CP, $Ti_3C_2$, NCP, and NCP/$Ti_3C_2$. The symbols "♠," "♣," and "♥" indicate the NP, CP, and $Ti_3C_2$ composites, respectively. (b) FTIR and (c) Raman spectra of NP, CP, $Ti_3C_2$, NCP, and NCP/$Ti_3C_2$. (d–k) XPS spectra of NCP/$Ti_3C_2$.

(Figure 2e) comprises three dominant contributions centered at 531.5, 533.5, and 535.5 eV, corresponding to lattice metal–oxygen bonds (Ni─O/Co─O/Ti─O), carbonyl (C═O), and mixed C─O/P═O species, respectively [40, 41]. These signals reflect the coexistence of metal oxides/hydroxides and phosphate-related moieties, which are known to participate in redox reactions and facilitate proton-coupled electron transfer.

The F1s spectrum (Figure 2f) displays components at 685.5, 687.5, and 688.5 eV, assigned to surface ─F terminations (F─C/C─Ti─$F_x$), residual Al─F, and Ti─F─Ti, respectively, indicating that partial F-termination of MXene persists after hybrid formation [42]. Such terminations often modulate interfacial wettability and pseudocapacitive kinetics. The C1s envelope (Figure 2g) shows well-resolved Ti─C, C─C, and C─O contributions at 285.18, 287.28, and 290.50 eV, confirming the integrity of the $Ti_3C_2$ backbone and the presence of surface oxygen functionalities [43]. The P2p spectrum (Figure 2h) exhibits the expected doublet at 133.5 ($2P_{3/2}$) and 135.6 eV ($2P_{1/2}$), consistent with oxidized phosphate species, suggesting strong interfacial coupling between NCP nanostructures and the MXene substrate [44]. The Co2p spectrum (Figure 2i) shows $Co^{2+}/Co^{3+}$ features

with characteristic spin-orbit doublets at 783.18 ($2p_{3/2}$) and 798.38 eV ($2p_{1/2}$), accompanied by satellite peaks at ~788.18 and 805.18 eV. These satellites are indicative of high-spin Co states commonly associated with electroactive layered oxyhydroxides [45–47].

Similarly, the Ti 2p region (Figure 2j) contains peaks at 456.08, 460.48, and 465.58 eV, attributable to Ti–F, Ti–O ($2p_{3/2}$), and Ti–O ($2p_{1/2}$), confirming partial surface oxidation alongside fluorinated sites [19, 48]. Such mixed surface terminations are known to enhance ion accessibility and interlayer charge transfer. Finally, the Ni2p spectrum (Figure 2k) shows $Ni^{2+}$/$Ni^{3+}$ doublets at 857.78 ($2p_{3/2}$) and 875.58 eV ($2p_{1/2}$), together with satellites of $Co2p_{3/2}$ and $Co2p_{1/2}$ at 862.18 and 879.78 eV, respectively [47, 49]. The coexistence of multiple oxidation states highlights the redox-active nature of Ni and Co sites within the hybrid, which collectively contribute to the enhanced pseudocapacitive performance.

## 3.2 | Morphology Studies

FESEM was used to analyze the structural characteristics of the samples in their as-prepared state. Figure 3a shows the FESEM image of CP, which exhibits an irregular, plate-like structure. In contrast, the FESEM image of NP in Figure 3b reveals an

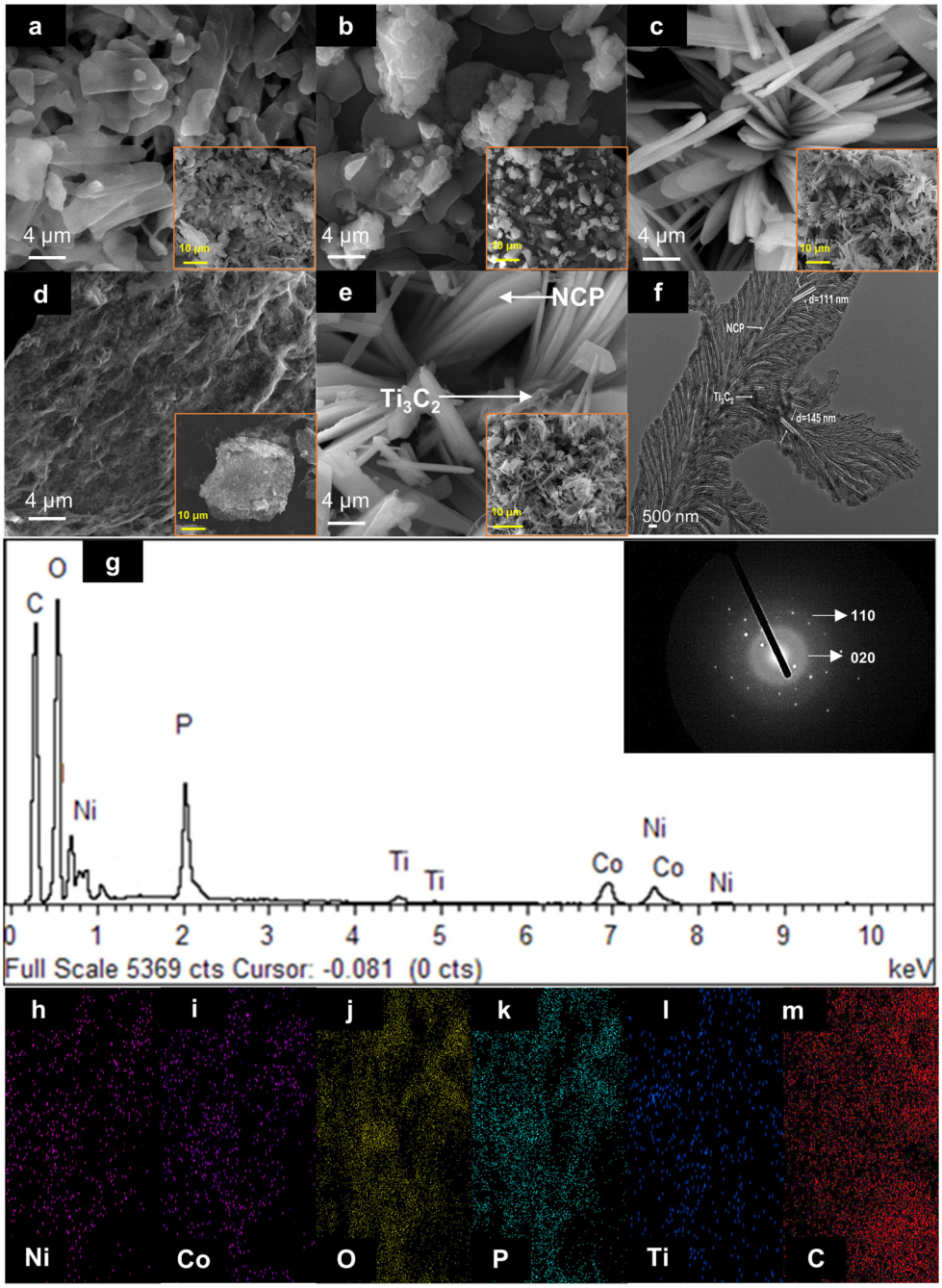


**FIGURE 3** | High magnification FESEM images of (a) CP, (b) NP, (c) NCP, (d) $Ti_3C_2$, and (e) NCP/$Ti_3C_2$. The inset shows low-magnification FESEM images of the as-prepared composites. (f) TEM image and (g) EDX spectrum of NCP/$Ti_3C_2$. Inset shows the SAED pattern of NCP/$Ti_3C_2$. (h–m) Elemental mapping of NCP/$Ti_3C_2$.

aggregated, irregular morphology. Remarkably, the microwave-assisted combination of CP and NP precursors resulted in a unique flower-like morphology for the NCP sample. The FESEM images show that the NCP structure lacks the agglomerated features observed for NP. Instead, NCP possesses an open, porous architecture that is likely advantageous for ion diffusion and electron transport kinetics during electrocatalysis [12]. As shown in Figure 3d, $Ti_3C_2$ exhibits a nanosheet-like morphology, demonstrating that $Ti_3C_2$-MXene was successfully delaminated and exfoliated. Notably, the addition of $Ti_3C_2$ to NCP to produce NCP/$Ti_3C_2$ did not alter its morphology. The presence of both the flower-like morphology of NCP and nanosheet-like morphology of $Ti_3C_2$ (Figure 3e) is expected to produce a synergistic effect and boost the electrochemical performance of the NCP/$Ti_3C_2$ electrode. In addition, the insets of Figure 3a–e show low-resolution FESEM images, which confirm the uniform distribution of the composite materials. HRTEM and selected area electron diffraction pattern (SAED) analyses were conducted to further confirm the structure and crystallinity of the as-prepared NCP/$Ti_3C_2$ electrode. The findings revealed clear and observable lattice fringes, which signified the successful preparation of the NCP/$Ti_3C_2$ electrode (Figure 3f). The larger lattice fringe is attributed to the NCP, while the smaller one is ascribed to the exfoliated $Ti_3C_2$. The presence of both NCP and $Ti_3C_2$ is expected to enhance the electrochromic and supercapacitive properties of NCP/$Ti_3C_2$ electrode. The resulting SAED patterns (Figure 3g, inset) demonstrate that the as-prepared NCP/$Ti_3C_2$ electrode was polycrystalline owing to the existence of a distinct diffraction loop, which may be indexed to the (002) and (110) planes of CP. The SAED patterns were consistent with the XRD results. Figure 3g shows the EDX spectrum of the NCP/$Ti_3C_2$ electrode, with peaks corresponding to the elements present in NCP/$Ti_3C_2$, confirming its successful formation. Elemental mapping analysis (Figure 3h–m) established the existence of all elements in the NCP/$Ti_3C_2$ electrode, indicating the successful deposition of these elements.

### 3.3 | ANOVA of NCP/$Ti_3C_2$

The fabrication of NCP/$Ti_3C_2$ electrodes was systematically optimized using CCD within the RSM framework. As detailed in Table 2, 11 experimental trials were conducted by varying $Ti_3C_2$ and NCP concentrations to evaluate specific capacitance and validate the predictive accuracy of the surface response model. The reduced quadratic model, selected through RSM analysis, demonstrated robust statistical reliability with an $R^2$ value of 0.9966 (Table 3), confirming its ability to explain 99.66% of the variance in the data set. The model's significance ($p < 0.05$) and the negligible lack-of-fit term ($p > 0.05$) further validate its suitability for predicting electrode performance [50, 51]. Among the model terms, factors $A$ ($Ti_3C_2$ concentration), $B$ (NCP concentration), and their quadratic interactions ($A^2$, $B^2$) exhibited statistically significant contributions, highlighting their critical roles in modulating specific capacitance. The optimization constraints (Table 4) yielded an NCP/$Ti_3C_2$ electrode with a specific capacitance of 655.98 F/g, which was consistent with the model prediction. The residual standard error (RSE) of 0.04% (Table 5) highlights the precision of the model, while an average RSE of 0.83% across triplicate validations reflects a predictive accuracy of 99.17%. These results confirm the reliability of the model as a quantitative tool for guiding electrode synthesis and performance optimization.

The diagnostic plots in Figure 4a (normal probability plot of residuals) and Figure 4b (predicted vs. actual values) corroborate the model's validity. The linear distribution of residuals in Figure 4a confirms the normality of the error distribution, whereas the tight clustering of data along the regression line in Figure 4b reinforces the predictive reliability of the model. Figure 4c shows a perturbation plot illustrating the sensitivity of the specific capacitance to perturbations in $Ti_3C_2$ ($A$) and NCP ($B$) concentrations, aligning with the statistical significance of these factors. The quadratic relationship between variables is further evidenced by the elliptical contours in the 2D contour plot (Figure 4d) and the pronounced curvature of the 3D response surface (Figure 4e). These features indicate a synergistic interaction between the $Ti_3C_2$ and NCP concentrations, wherein simultaneous adjustments amplify specific capacitance. This behavior aligns with the significance of the quadratic terms ($A^2$, $B^2$) in the derived regression equation (Equation 6). The strong interdependence between these parameters, as shown in Figure 4e, highlights the necessity of balanced optimization to maximize electrode performance.

**TABLE 2** | Experimental and predicted specific capacitance of NCP/$Ti_3C_2$ electrode via RSM/CCD.

| Run | *A*: Concentration of $Ti_3C_2$ (mg/mL) | *B*: Concentration of NCP (mg/mL) | Specific capacitance (F/g) | |
|---|---|---|---|---|
| | | | Experimental | Predicted |
| 1 | 3 | 100 | 439.141 | 464.72 |
| 2 | 2 | 100 | 655.98 | 618.27 |
| 3 | 2 | 20 | 394.366 | 405.07 |
| 4 | 3 | 180 | 192.161 | 170.13 |
| 5 | 1 | 180 | 153.937 | 128.29 |
| 6 | 1 | 100 | 383.363 | 416.17 |
| 7 | 2 | 100 | 645.483 | 618.27 |
| 8 | 2 | 180 | 279.344 | 327.03 |
| 9 | 3 | 20 | 258.41 | 254.87 |
| 10 | 2 | 100 | 611.726 | 618.27 |
| 11 | 1 | 20 | 206.788 | 199.63 |

**TABLE 3** | ANOVA for NCP/$Ti_3C_2$ synthesis.

| Source | Sum of squares | df | Mean square | *F*-value | *p* value | |
|---|---|---|---|---|---|---|
| Model | 0.4894 | 5 | 0.0979 | 288.93 | < 0.0001 | Significant |
| *A* | 0.0106 | 1 | 0.0106 | 31.27 | 0.0025 | Significant |
| *B* | 0.0276 | 1 | 0.0276 | 81.33 | 0.0003 | Significant |
| *AB* | 5.306E-8 | 1 | 5.306E-8 | 0.0002 | 0.9905 | |
| $A^2$ | 0.1087 | 1 | 0.1087 | 320.76 | < 0.0001 | Significant |
| $B^2$ | 0.2268 | 1 | 0.2268 | 669.42 | < 0.0001 | Significant |
| Residual | 0.0017 | 5 | 0.0003 | | | |
| Lack of fit | 0.0012 | 3 | 0.0004 | 1.57 | 0.4116 | Not significant |
| Pure error | 0.0005 | 2 | 0.0003 | | | |
| Cor total | 0.4911 | 10 | | | | |
| Standard deviation | 0.0184 | | | | | |
| Mean | 2.53 | | | | | |
| Coefficient of variation | 0.7262 | | | | | |
| $R^2$ | 0.9966 | | | | | |
| Adjusted $R^2$ | 0.9931 | | | | | |
| Predicted $R^2$ | 0.9769 | | | | | |
| Adequate precision | 45.3136 | | | | | |

**TABLE 4** | Optimization parameters goal.

| | | Limit | |
|---|---|---|---|
| **Name** | **Goal** | **Lower** | **Upper** |
| Molarity of $Ti_3C_2$ (mg/mL) | Within limits | 1 | 3 |
| Molarity of NCP (mg/mL) | Within limits | 20 | 180 |
| Specific capacitance (F/g) | Maximize | 153.937 | 655.98 |

**TABLE 5** | Predicted and experimental specific capacitance and RSE conducted under optimum conditions.

| | | | Specific capacitance (F/g) | | |
|---|---|---|---|---|---|
| **Solution** | **Concentration of $Ti_3C_2$ (mg/mL)** | **Concentration of NCP (mg/mL)** | **Predicted** | **Experiment** | **RSE (%)** |
| 1 | 2.1019 | 90.9419 | 655.727 | 655.980 | 0.04 |
| 2 | 2.1019 | 90.9419 | 655.727 | 645.483 | 1.56 |
| 3 | 2.1019 | 90.9419 | 655.727 | 649.914 | 0.89 |

$$\begin{aligned}\mathrm{Log}_{10}\text{specific capacitance} = {} & +1.51519 + (0.870606\mathrm{A}) \\ & + (0.008506\mathrm{B}) \\ & - (1.43968 \times 10^{-6}\mathrm{AB}) \\ & - (0.207111\mathrm{A}^2) - (0.000047\mathrm{B}^2).\end{aligned} \quad (6)$$

## 3.4 | Electrochemical Studies

Figure 5a shows the absorbance spectra of the NCP/$Ti_3C_2$ electrode at three different potentials (0, 0.3, and 0.5 V), and the inset of Figure 5a shows a digital photograph of the different applied voltages. The findings indicate that the highest potential (0.5 V) corresponds to the highest absorbance intensity due to the darker color (black) of the electrode material. Conversely, the lowest potential (0 V) displayed the lowest absorbance intensity owing to the light color (bright green) of NCP/$Ti_3C_2$ at low voltages. Interestingly, the transmittance spectra (Figure 5b) show a trend opposite to that of the absorbance spectra. This is because the electrode material is less opaque at low applied voltages than that at high voltages [10, 12]. Notably, the NCP/$Ti_3C_2$ electrode showed a high CE of 132.68 $cm^2$/C, which is analogous to MXene-based electrochromic materials such as NW/$P_2W_{17}Ni/Ti_3C_2T_x$ (30.7 $cm^2$/C) [52], $V_2CT_x$ MXene (91.1 $cm^2$/C) [53], FTO-$P_5W_{30}/Ti_3C_2T_x$ (77.48 $cm^2$/C) [54], $WO_3/Ti_3C_2T_x$ MXene (126.00 $cm^2$/C) [55], and NCP/$V_2CT_x$ (104.00 $cm^2$/C) [56] (Table 6). Transmittance spectra versus

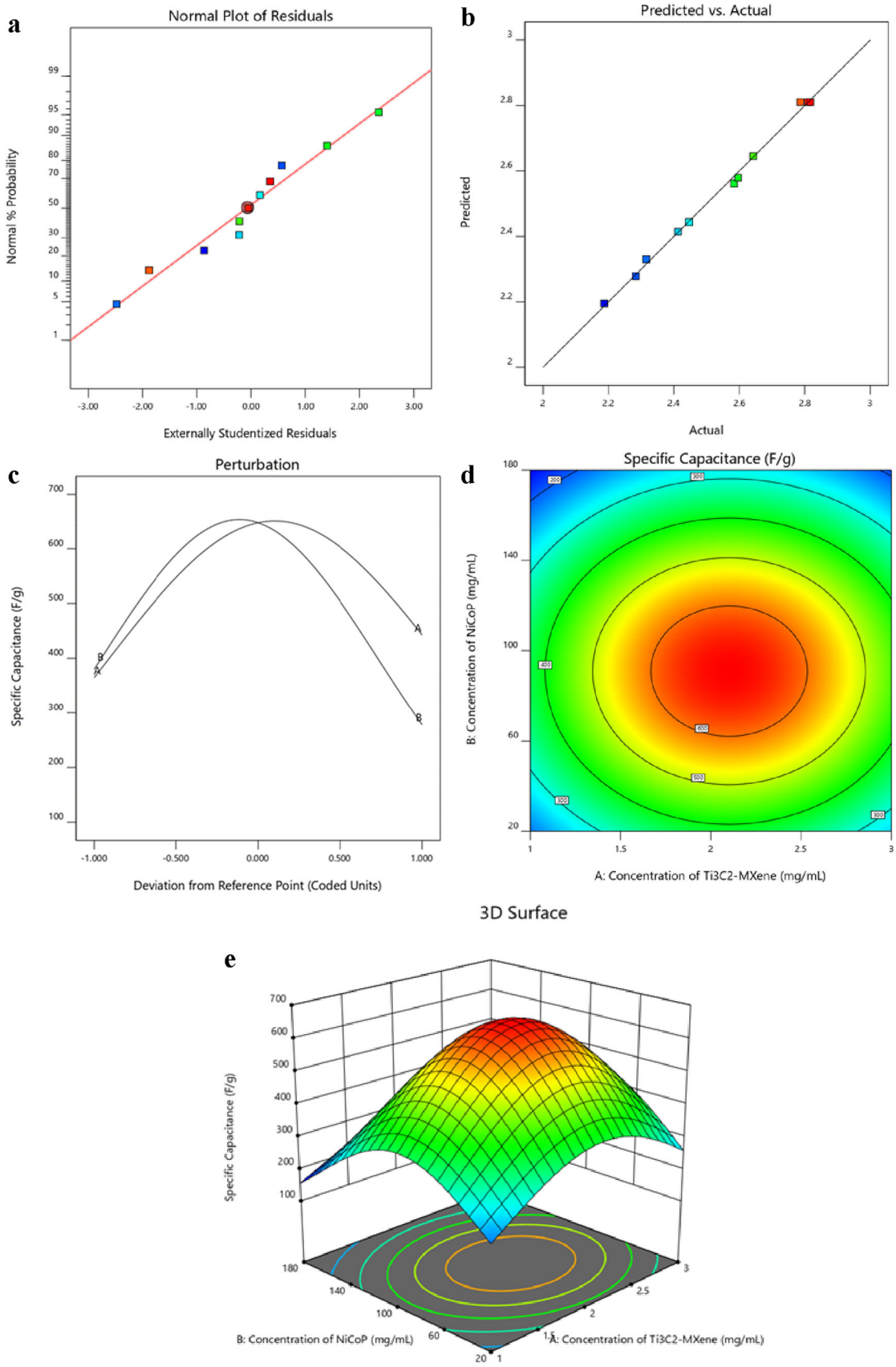


**FIGURE 4** | (a) Normal plot of residual, (b) predicted versus actual, (c) perturbation plot, (d) 2D surface plot, and (e) 3D surface plot.

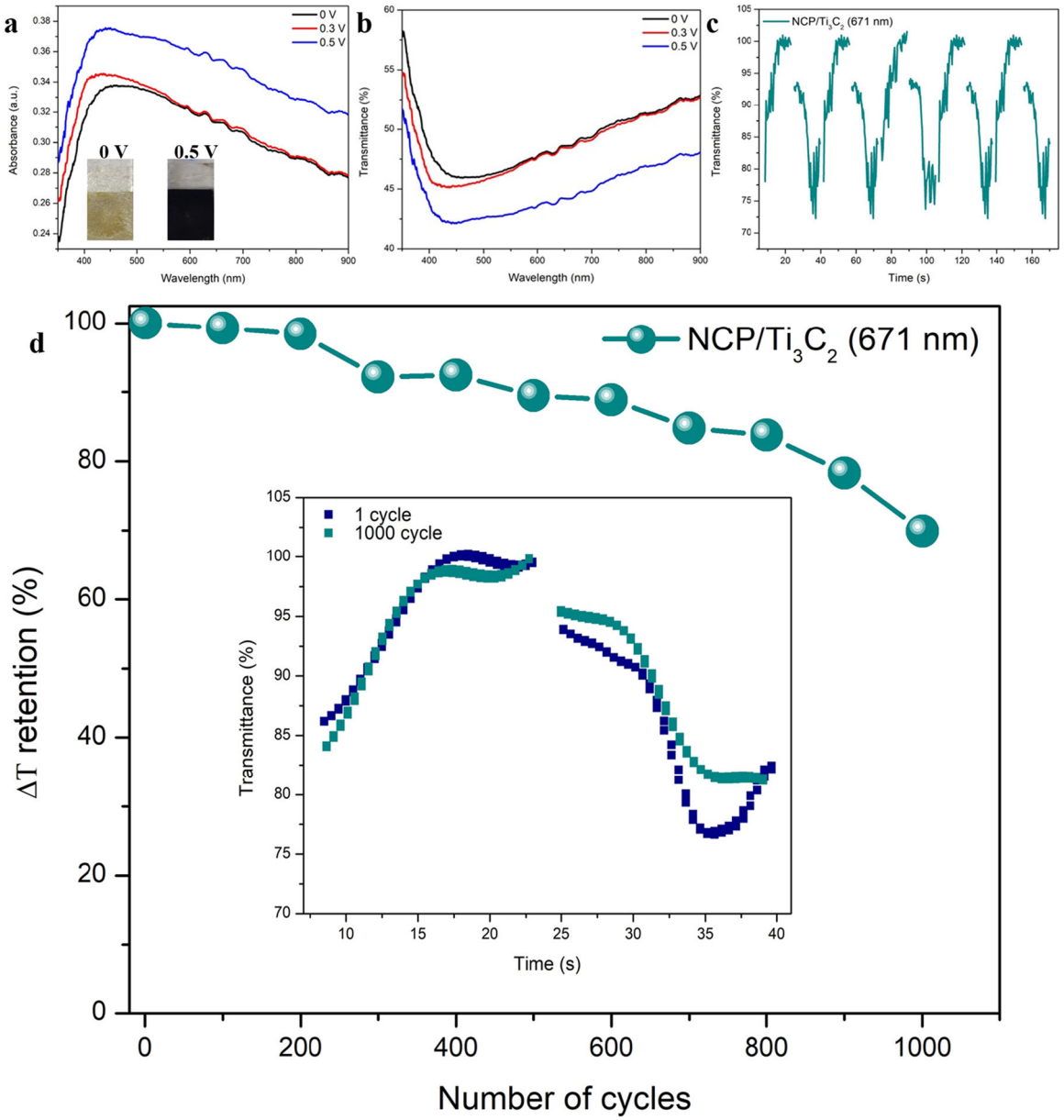


**FIGURE 5** | (a) Absorbance versus wavelength. Inset shows digital photographs of NCP/$Ti_3C_2$ at 0 and 0.5 V. (b) Transmittance of NCP/$Ti_3C_2$ as a function of wavelength. (c) Transmittance of NCP/$Ti_3C_2$ as a function of time at 671 nm. (d) Optical contrast retention at 671 nm for 1000 cycles. The insets show the first and 1000th cycles of transmittance versus time.

**TABLE 6** | Electrochromic performance of NCP/$Ti_3C_2$ electrode compared with state-of-the-art systems.

| Material | CE ($cm^2$/C) | $\Delta T$ (%) | Stability (%) | References |
|---|---|---|---|---|
| NW/$P_2W_{17}Ni$/$Ti_3C_2T_x$ | 30.70 | 9.30 | — | [52] |
| $V_2CT_x$ MXene | 91.10 | 53.98 | 83.70 (200 cycles) | [53] |
| FTO-$P_5W_{30}$/$Ti_3C_2T_x$ | 77.48 | 16.80 | — | [54] |
| $WO_3$/$Ti_3C_2T_x$ MXene | 126.00 | 57.61 | — | [55] |
| NCP/$V_2CT_x$ | 104.00 | 30.85 | 64.29 (1000 cycles) | [56] |
| NCP/$Ti_3C_2$ | 132.68 | 28.69 | 75.00 (1000 cycles) | This study |

time (Figure 5c) were performed to analyze the $\Delta T$, $t_c$, and $t_b$. The findings show that the NCP/$Ti_3C_2$ electrode is capable of achieving a moderate $\Delta T$ of 28.69%, a fast $t_c$ of 13.16 s, and a fast $t_b$ of 13.04 s, signifying the remarkable electrochromic performance of electrode materials. Furthermore, the optimized NCP/$Ti_3C_2$ electrode was subjected to stability tests (Figure 5d), and the findings showed a remarkable retention of 75% even after 1000th cycles. Figure 5d (inset) shows the transmittance spectra

for the first and 1000th cycles. Overall, the NCP/$Ti_3C_2$ electrode can be regarded as a good material for electrochromic applications due to its fast switching time and good $\Delta T$ retention.

The electrochemical behavior of the synthesized NCP/$Ti_3C_2$ composite was evaluated and compared with that of pristine NCP and $Ti_3C_2$ to elucidate the synergistic contributions of both components. Figure 6a shows the CV profiles, where the NCP/$Ti_3C_2$ electrode exhibited the largest enclosed area and most pronounced redox features. This enhancement indicates a higher charge storage capability arising from the improved electrical conductivity and increased number of electroactive

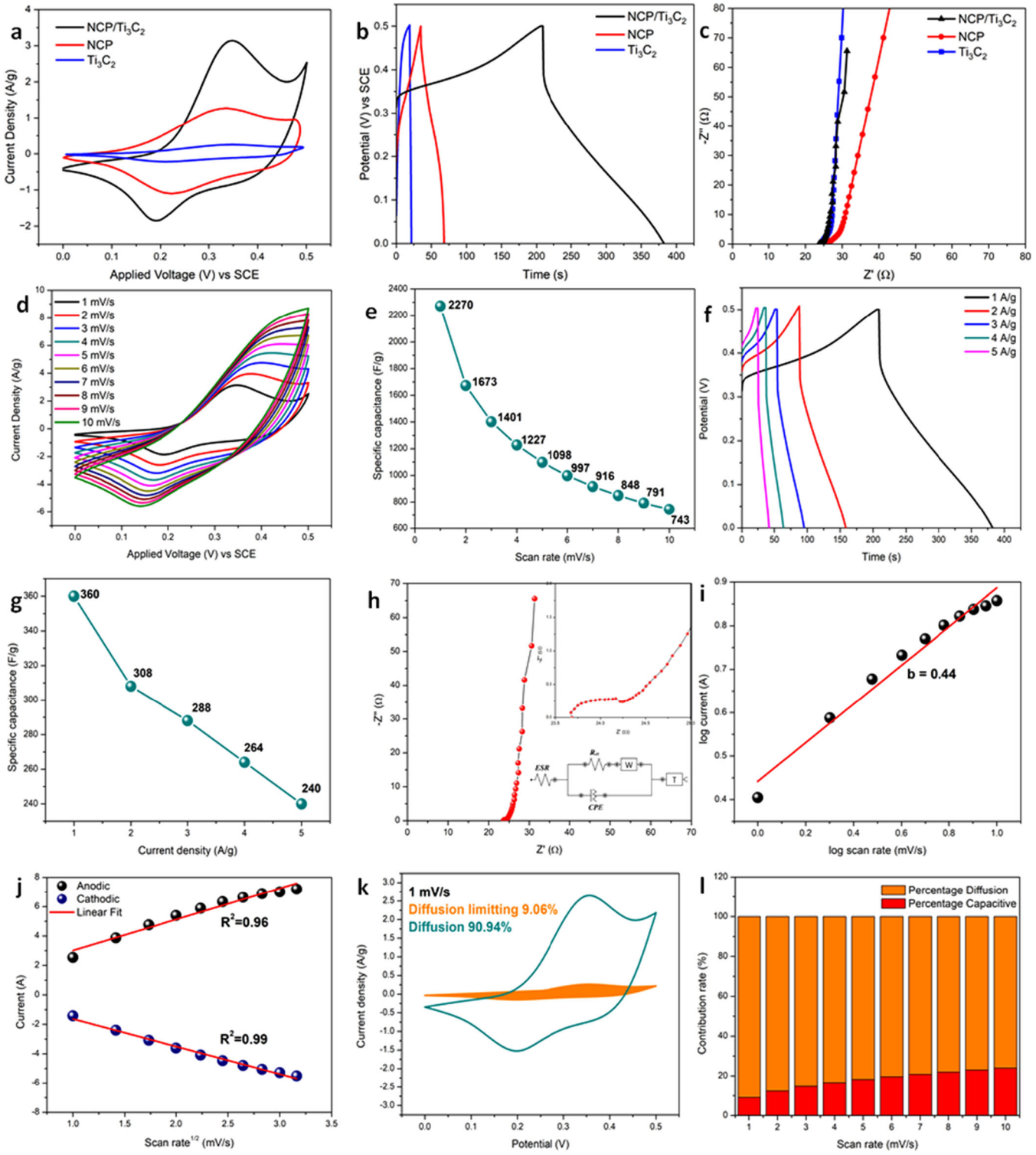


**FIGURE 6** | (a–c) CV curves, GCD curvature, and Nyquist plot of NCP/$Ti_3C_2$, NCP, and $Ti_3C_2$, respectively. (d) CV curves of NCP/$Ti_3C_2$ at multiple scan rates (1–10 mV/s), (e) line graph of $C_{sp}$ versus scan rates (1–10 mV/s), (f) GCD curves of NCP/$Ti_3C_2$ at multiple scan rates (1–5 A/g), (g) line graph of $C_{sp}$ versus current densities (1–5 A/g), and (h) Nyquist graph of NCP/$Ti_3C_2$. Inset shows high magnification of the Nyquist graph and the circuit. (i–l) Dunn method analysis of NCP/$Ti_3C_2$ at multiple scan rates (1–10 mV/s).

sites introduced by the integration of $Ti_3C_2$ MXene [57]. In contrast, pristine NCP and $Ti_3C_2$ exhibited weaker redox peaks and lower current responses. The broadened and intensified redox peaks of the NCP/$Ti_3C_2$ composite confirm that the interfacial coupling between NCP and $Ti_3C_2$ promotes fast faradaic reactions while maintaining capacitive buffering, resulting in a hybrid charge-storage mechanism [57]. The GCD curves shown in Figure 6b further support this observation. The NCP/$Ti_3C_2$ electrode displayed the longest discharge time, indicating a substantially higher specific capacity than that of the individual components. The visible voltage plateau suggests a predominant faradaic contribution, which is more stable and extended for the NCP/$Ti_3C_2$ composite. In contrast, both NCP and $Ti_3C_2$ exhibited very short discharge durations. The improved kinetics and prolonged discharge of NCP/$Ti_3C_2$ reflect the reduced internal resistance and more efficient electron transport pathways facilitated by the conductive MXene layers [10]. The EIS results (Figure 6c) provide further insights into the interfacial and transport characteristics. The NCP/$Ti_3C_2$ electrode exhibited the smallest semicircle diameter in the high-frequency region compared to pristine NCP and pristine $Ti_3C_2$, corresponding to the lowest charge-transfer resistance ($R_{ct}$). This outcome highlights the role of $Ti_3C_2$ in enhancing electronic conductivity and improving the electrode–electrolyte interface [58]. Additionally, the steeper slope in the low-frequency region indicates superior diffusion behavior and faster ion transport within the NCP/$Ti_3C_2$ composite. Overall, the combined CV, GCD, and EIS analyses demonstrated that the NCP/$Ti_3C_2$ composite exhibited significantly improved electrochemical performance compared to its individual constituents. The enhanced redox activity, prolonged discharge stability, reduced charge transfer resistance, and improved ion diffusion collectively confirm the strong synergistic interaction between NCP and $Ti_3C_2$. This synergy enables faster reaction kinetics and more efficient charge storage, making the composite a promising electrode material for high-performance energy-storage applications.

Figure 6d shows the cyclic voltammograms of the NCP/$Ti_3C_2$ electrode recorded at scan rates ranging from 1 to 10 mV/s. Measurements were conducted in a 3ES configuration comprising a platinum counter electrode, an SCE, and the NCP/$Ti_3C_2$ working electrode immersed in 1 M LiOH aqueous electrolyte. The voltammograms exhibited well-defined and scan rate-independent profiles, with no discernible shifts in the anodic or cathodic features. The pronounced redox couple observed at low scan rates indicates battery-type charge storage, which is consistent with previous reports [10, 12]. As the scan rate increases, the redox signature becomes progressively attenuated, likely reflecting the kinetic limitations associated with ion diffusion and restricted electrolyte penetration into the electrode architecture at higher sweep speeds [10, 12]. This behavior correlates with a substantial decrease in the stored charge, from 2270 F/g at 1 mV/s to 743 F/g at 10 mV/s (Figure 6e). Complementary galvanostatic charge–discharge measurements performed at current densities from 1 to 5 A/g using the same 3ES (Figure 6f) revealed mildly plateaued profiles, further substantiating the battery-type electrochemical response of the NCP/$Ti_3C_2$ electrode [10, 12]. Notably, the GCD curve also achieved 0.5 V, which is consistent with the potential window of CV analysis. Additionally, the discharging time decreased with increasing current densities, which reduced the specific capacitance at higher current densities (Figure 6g). In summary, both CV and GCD analyses showed a reduction in specific capacitance at high sweeping rates and high current densities, respectively, due to the behavior of electrolyte ions that did not have enough time to penetrate the bulk of the NCP/$Ti_3C_2$ electrode. EIS was performed in the same 3ES as CV and GCD to determine the resistance of the NCP/$Ti_3C_2$ electrode (Figure 6h). The equivalent circuit (Figure 6h, inset) consists of an equivalent series resistance (ESR), $R_{ct}$, constant phase element (CPE), Warburg line (W), and tangent line (T). It is important to highlight that the fitting of this equivalent circuit yielded a remarkably low chi-square value ($7.04 \times 10^{-5}$), demonstrating an excellent fit of the circuit to the experimental data. Furthermore, a low $R_{ct}$ (1.2 Ω) indicates fast reaction kinetics between the electrode materials and electrolytes, whereas a moderate ESR (23.92 Ω) indicates a low internal resistance [59, 60]. In addition, a straight Warburg line almost perpendicular to the $x$-axis represents the capacitive behavior of electrode materials [59, 60]. In addition to CV, GCD, and EIS analyses, the Dunn method is important for studying the contribution of diffusion reactions to charge storage. The contribution ratios of the diffusion-controlled and diffusion-limiting reactions were evaluated using CV curves at diverse sweep rates. Equations (7) and (8) were used to perform Dunn's method.

$$i = av^b, \tag{7}$$

$$i(V) = k_1 v + k_2 v^{1/2} or \frac{i(V)}{v^{1/2}} = k_1 v^{1/2} + k_2, \tag{8}$$

where $i$ represents the current response, $i(V)$ denotes the current at a fixed potential, and $v$ is the scan rate, while $a$, $b$, $k_1$, and $k_2$ are fitting parameters used to describe the electrochemical process. The relationship between log(current) and log(scan rate), as shown in Figure 6i, is commonly used to determine the $b$-value. A $b$-value close to 0.5 indicates a diffusion-controlled process, whereas a value approaching 1 indicates a surface-controlled (capacitive) process [45]. As shown in Figure 6i, a $b$-value of 0.44 was obtained, confirming that the NCP/$Ti_3C_2$ electrode predominantly underwent a diffusion-controlled process. Figure 6j shows the anodic and cathodic peaks for the NCP/$Ti_3C_2$ electrode, which shows a linear relationship, signifying that the electrode materials mainly undergo a diffusion-controlled process [45]. Notably, the anodic and cathodic peaks for the NCP/$Ti_3C_2$ electrode also exhibited an $R^2$ value close to 1, indicating a reversible capability and confirming the battery-grade property of the NCP/$Ti_3C_2$ electrode [45]. Figure 6k shows the CV curves distinguishing the diffusion- and diffusion-limited-controlled processes. The analysis revealed that the NCP/$Ti_3C_2$ electrode exhibited predominantly diffusion-controlled behavior, accounting for 90.94% of the process (green), while the diffusion-limited contribution was only 9.06% (orange), consistent with the previously determined $b$- and $R^2$-values. Figure 6l further quantifies the contribution at various scan rates (1–10 mV/s). As the scan rate increased, the proportion of diffusion-controlled processes decreased, reflecting the inherently slower kinetics of diffusion-limited mechanisms compared to the faster diffusion-limiting processes [45].

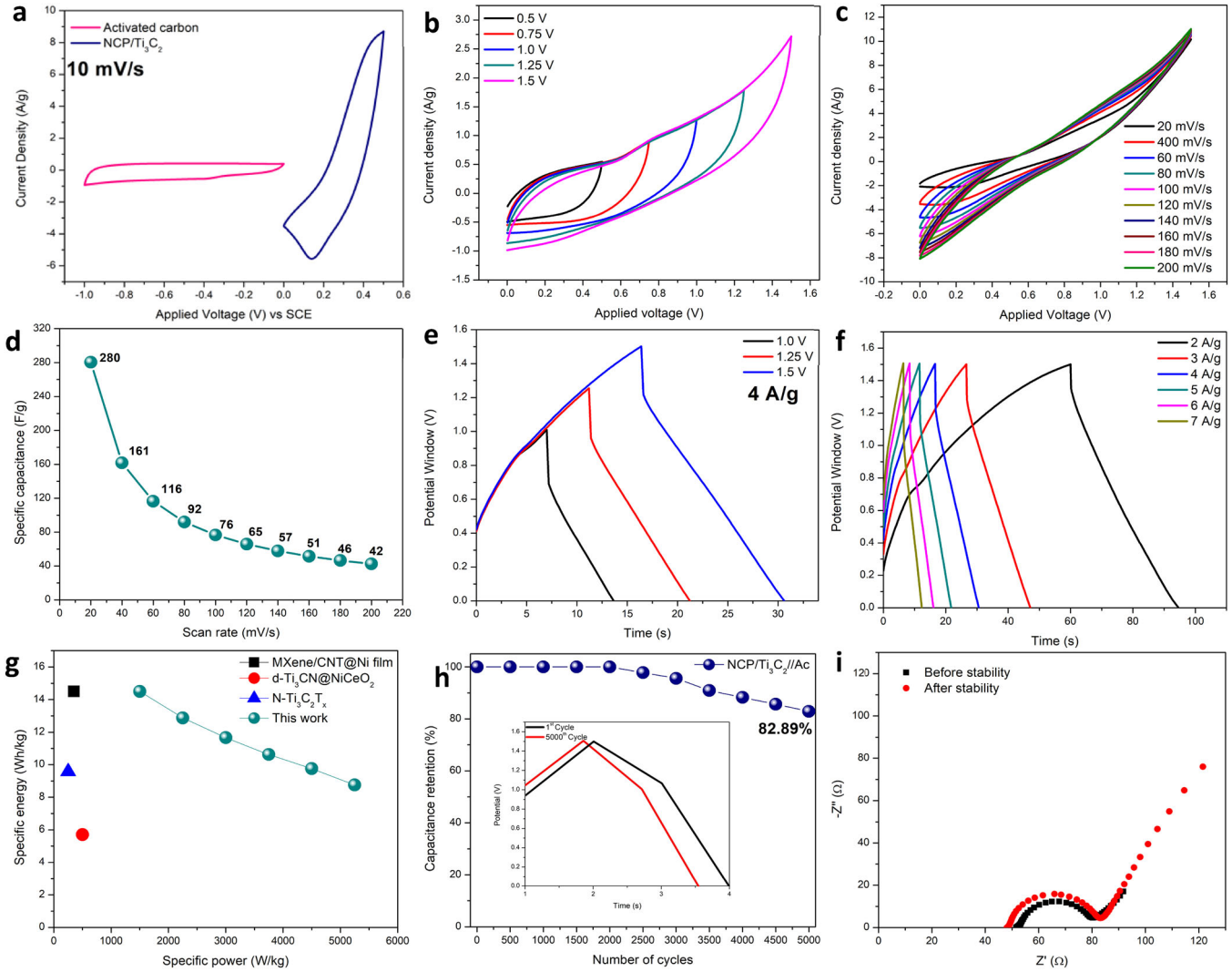


**FIGURE 7** | (a) CV curves of AC and NCP/$Ti_3C_2$ at 10 mV/s, (b) CV curves of NCP/$Ti_3C_2$//AC at different potential windows, (c) CV curves of NCP/$Ti_3C_2$//AC at various current densities (20–200 mV/s), (d) Line graph of $C_{sp}$ of NCP/$Ti_3C_2$//AC versus scan rates, (e) GCD curves of NCP/$Ti_3C_2$//AC at various potential windows, (f) GCD curves of NCP/$Ti_3C_2$//AC at several current densities (2–7 A/g), (g) Ragone plot of NCP/$Ti_3C_2$//AC in comparison with reported literature, and (h) Stability retention of NCP/$Ti_3C_2$//AC at 5000th cycle. The inset shows the GCD curves of NCP/$Ti_3C_2$//AC at the first and 5000th cycles. (i) Nyquist graph of NCP/$Ti_3C_2$//AC before and after stability.

This consequence is in concord with the CV analysis, where the redox peaks became less prominent upon increasing sweeping rates, signifying a reduction in the diffusion-controlled process at high scan rates.

Figure 7 shows the CV curves of the AC and NCP/$Ti_3C_2$ electrodes at 10 mV/s. AC was used as the negative electrode, and NCP/$Ti_3C_2$ was used as the positive electrode. The AC electrode exhibited the behavioral characteristics of an EDLC, whereas the NCP/$Ti_3C_2$ electrode exhibited properties comparable to those of a battery. By combining these materials in the NCP/$Ti_3C_2$//AC device, the synergistic effect of the high theoretical specific capacitance of NCP/$Ti_3C_2$ and the excellent stability of AC can be realized. As shown in Figure 7b, CV analysis was performed at different operating voltages to observe the capabilities of the electrode material to achieve certain potential windows. Consequently, the NCP/$Ti_3C_2$//AC device has the potential to reach a maximum operating voltage of 1.5 V. Furthermore, the NCP/$Ti_3C_2$//AC device underwent CV analysis at different scanning rates (20-200 mV/s) to calculate the charge storage capacity of the NCP/$Ti_3C_2$//AC device (Figure 7c). Figure 7d shows the line graph of specific capacitance at various scan rates, and the findings show that the NCP/$Ti_3C_2$//AC device can achieve a specific capacitance of 280 F/g at 20 mV/s. Notably, the line graph shows a decreasing trend in the specific capacitance with increasing scanning rates for the same reason described earlier in the 3ES CV analysis. As shown in Figure 7e, GCD at different operating voltages was performed to validate the outcomes of Figure 7b, and the results showed agreement between both analyses. GCD analysis was also performed at different current densities (2–7 A/g) to estimate the specific energy and specific power of the as-prepared NCP/$Ti_3C_2$//AC device.

As a result, the NCP/$Ti_3C_2$//Ac device produced a high energy density of 14.5 Wh/kg at a power density of 1500 W/kg (2 A/g). In addition, at high current densities (7 A/g), the NCP/$Ti_3C_2$//AC device maintained a high energy density of 8.75 Wh/kg at a power density of 5250 W/kg. Notably, the energy density and

**TABLE 7** | Comparison of the energy density, power density, and stability of the NCP/$Ti_3C_2$//AC device with previously reported studies.

| Material | Energy density (Wh/kg) | Power density (W/kg) | Current density (A/g) | References |
|---|---|---|---|---|
| MXene/CNT@Ni | 14.5 | 350 | 0.5 | [61] |
| d-$Ti_3CN$@$NiCeO_2$ | 5.7 | 500 | 1 | [62] |
| N-$Ti_3C_2T_x$ | 9.57 | 250 | 0.5 | [63] |
| MXene/$MoO_3$ | 13.4 | 534.6 | — | [64] |
| MXene/rGO | 10.5 | 80.3 | — | [65] |
| $MnO_2$/$Ti_3C_2$ | 8.3 | 221.3 | 1 | [66] |
| NCP/$Ti_3C_2$//AC | 14.50 | 1500 | 2 | This study |
| NCP/$Ti_3C_2$//AC | 8.75 | 5250 | 7 | This study |

power density achieved are comparable with the other published literature on MXene based devices such as MXene/CNT@Ni film (14.5 Wh/kg, 350 W/kg) [61], d-$Ti_3CN$@$NiCeO_2$ (5.7 Wh/kg, 500 W/kg) [62], N-$Ti_3C_2T_x$ (9.57 Wh/kg, 250 W/kg) [63], MXene/$MoO_3$ (13.4 Wh/kg, 534.6 W/kg) [64], MXene/rGO (10.5 Wh/kg, 80.3 W/kg) [65], and $MnO_2$/$Ti_3C_2$ (8.3 Wh/kg, 221.3 W/kg) [66] (Table 7). Figure 7h shows the stability test of the NCP/$Ti_3C_2$//Ac device. Notably, the NCP/$Ti_3C_2$//AC device preserved 82.89% of its initial capacitance after 5000 cycles. The NCP/$Ti_3C_2$//AC device was stable during the first 2000 cycles but gradually degraded in performance thereafter. This decline can be attributed to the faradaic charge-storage mechanism inherent to the NCP/$Ti_3C_2$ electrode, where repeated redox reactions induce structural strain, surface oxidation, and partial detachment of the active material from the current collector [67, 68]. The NCP/$Ti_3C_2$//AC device thus undergoes progressive mechanical and interfacial wear owing to the recurring insertion and extraction of electrolyte ions during charge–discharge processes [67, 68]. As illustrated in the inset of Figure 7h, the GCD curves of the first and 5000th cycles reveal a slightly larger IR drop and shorter discharge duration after cycling, indicating an increase in internal resistance and reduced electrochemical reversibility. Similarly, the Nyquist plots (Figure 7i) show that the Warburg line became slightly longer and the semicircle diameter marginally increased after cycling, signifying higher charge-transfer resistance and slower ion diffusion. These observations confirm that the gradual capacitance fading mainly originates from the faradaic reaction-driven degradation of the NCP/$Ti_3C_2$ electrode and the accompanying increase in interfacial resistance.

## 4 | Conclusion

The NCP/$Ti_3C_2$ electrode was successfully synthesized using versatile microwave and spin-coating techniques. The NCP/$Ti_3C_2$ electrode was optimized using RSM/CCD to enhance both its electrochromic and supercapacitor performance. Based on the optimization tool, the NCP/$Ti_3C_2$ electrodes exhibited excellent surface response predictability with an average RSE of 0.83% and a good model predictability of up to 99.17%. In addition, the 3ES study comprising CV, GCD, and EIS concluded that NCP/$Ti_3C_2$ is an excellent electrode material in electrochromic and supercapacitor applications owing to the high specific capacitance generated and low resistance produced. Dunn analysis further confirmed that the NCP/$Ti_3C_2$ electrode mainly undergoes a diffusion-controlled process. Furthermore, the 2ES study revealed that the NCP/$Ti_3C_2$//AC device possessed excellent specific capacitance, high specific energy, high specific power, and good stability retention. All analyses, including 3ES and 2ES, confirmed the potential of NCP/$Ti_3C_2$ electrodes for implementation as multifunctional energy storage devices. Future work may focus on integrating the NCP/$Ti_3C_2$ electrode into practical electrochromic devices (e.g., smart windows) and exploring its suitability for wearable energy-storage systems. Emphasis should be placed on flexible substrates, durability testing, and pairing the electrode with solid-state or gel electrolytes to enable real-world implementation.


### Acknowledgments

The authors are grateful for the financial assistance from the Sunway University Research Grant (STR-RCGS-E_CITIES[S]-004-2022).


### Conflicts of Interest

The authors declare no conflicts of interest.

### Data Availability Statement

Data for the current study are available from the corresponding author upon reasonable request.

### References


1. Y. Martínez-Martínez, J. Dewulf, M. Aguayo, and Y. Casas-Ledón, "Sustainable Wind Energy Planning Through Ecosystem Service Impact Valuation and Exergy: A Study Case in South-Central Chile," *Renewable and Sustainable Energy Reviews* 178 (2023): 113252.

2. H. Miao, H. Xu, G. Huang, and K. Yang, "Evaluation and Future Projections of Wind Energy Resources Over the Northern Hemisphere in CMIP5 and CMIP6 Models," *Renewable Energy* 211 (2023): 809–821.

3. M. N. Mustafa, N. A. Azhari, and Y. Sulaiman, "Reduced Graphene Oxide-Titanium Dioxide Compact Layer Prepared via Electrodeposition for Enhanced Performance of Dye-Sensitized Solar Cells," *Optical Materials* 120 (2021): 111475.

4. M. N. Mustafa and Y. Sulaiman, "Fully Flexible Dye-Sensitized Solar Cells Photoanode Modified With Titanium Dioxide-Graphene Quantum Dot Light Scattering Layer," *Solar Energy* 212 (2020): 332–338.

5. M. N. Mustafa, S. Shafie, M. H. Wahid, and Y. Sulaiman, "Preparation of $TiO_2$ Compact Layer by Heat Treatment of Electrospun $TiO_2$ Composite for Dye-SensItized Solar Cells," *Thin Solid Films* 693 (2020): 137699.

6. N. Rezaei, Y. Pezhmani, and R. P. Mohammadiani, "Optimal Stochastic Self-Scheduling of a Water-Energy Virtual Power Plant Considering Data Clustering and Multiple Storage Systems," *Journal of Energy Storage* 65 (2023): 107366.

7. M. Abidi, A. B. Rhouma, and J. Belhadj, "Optimal Coordinated Planning of Water-Energy System-Based Milp Algorithm of a Multi-Pump PV Water Station by Deeming Power Commitment," *Electric Power Systems Research* 220 (2023): 109343.

8. J. Iqbal, A. Numan, R. Jafer, et al., "Ternary Nanocomposite of Cobalt Oxide Nanograins and Silver Nanoparticles Grown on Reduced Graphene Oxide Conducting Platform for High-Performance Supercapattery Electrode Material," *Journal of Alloys and Compounds* 821 (2020): 153452.

9. S. G. Krishnan, A. Arulraj, M. Khalid, M. V. Reddy, and R. Jose, "Energy Storage in Metal Cobaltite Electrodes: Opportunities & Challenges in Magnesium Cobalt Oxide," *Renewable and Sustainable Energy Reviews* 141 (2021): 110798.

10. M. N. Mustafa, M. A. A. Mohd Abdah, A. Numan, Y. Sulaiman, R. Walvekar, and M. Khalid, "Development of High-Performance MXene/Nickel Cobalt Phosphate Nanocomposite for Electrochromic Energy Storage System Using Response Surface Methodology," *Journal of Energy Storage* 68 (2023): 107880.

11. M. N. Mustafa, M. A. A. Mohd Abdah, A. Numan, A. Moreno-Rangel, A. Radwan, and M. Khalid, "Smart Window Technology and Its Potential for Net-Zero Buildings: A Review," *Renewable and Sustainable Energy Reviews* 181 (2023): 113355–113375.

12. M. N. Mustafa, M. A. A. M. Abdah, A. Numan, Y. Sulaiman, R. Walvekar, and M. Khalid, "Specific Capacity Optimization of Nickel Cobalt Phosphate Using Response Surface Methodology for Enhanced Electrochromic Energy Storage Performance," *Electrochimica Acta* 441 (2023): 141765.

13. M. N. Mustafa, N. H. N. Azman, and Y. Sulaiman, "Emerging Materials for Energy Applications," in *Handbook of Energy Materials*, ed. R. Gupta (Springer Nature Singapore, 2022), 1–19.

14. K.-S. Ahn, R. Vinodh, B. G. Pollet, et al., "A High-Performance Asymmetric Supercapacitor Consists of Binder Free Electrode Materials of Bimetallic Hydrogen Phosphate ($MnCo(HPO_4)$) Hexagonal Tubes and Graphene Ink," *Electrochimica Acta* 426 (2022): 140763.

15. A. A. Mirghni, K. O. Oyedotun, O. Fasakin, B. A. Mahmoud, D. J. Tarimo, and N. Manyala, "High-Performance Bimetallic Ni-Mn Phosphate Hybridized With 3-D Graphene Foam for Novel Hybrid Supercapacitors," *Journal of Energy Storage* 31 (2020): 101584.

16. Y. Tang, W. Guo, and R. Zou, "Nickel-Based Bimetallic Battery-Type Materials for Asymmetric Supercapacitors," *Coordination Chemistry Reviews* 451 (2022): 214242.

17. F. S. Omar, A. Numan, S. Bashir, et al., "Enhancing Rate Capability of Amorphous Nickel Phosphate Supercapattery Electrode via Composition With Crystalline Silver Phosphate," *Electrochimica Acta* 273 (2018): 216–228.

18. M. A. A. M. Abdah, H. T. A. Awan, M. Mehar, et al., "Advancements in MXene-Polymer Composites for High-Performance Supercapacitor Applications," *Journal of Energy Storage* 63 (2023): 106942.

19. M. A. A. M. Abdah, J. Cherusseri, N. A. Dzulkarnain, et al., "Facile Synthesis of Microwave-Etched $Ti_3C_2$ MXene/Activated Carbon Hybrid for Lithium-Ion Battery Anode," *Journal of Electroanalytical Chemistry* 928 (2023): 117050–117060.

20. Y. Tang, J. Zhu, C. Yang, and F. Wang, "Enhanced Supercapacitive Performance of Manganese Oxides Doped Two-Dimensional Titanium Carbide Nanocomposite in Alkaline Electrolyte," *Journal of Alloys and Compounds* 685 (2016): 194–201.

21. J. Chen, Y. Ren, H. Zhang, J. Qi, Y. Sui, and F. Wei, "Ni-Co-Fe Layered Double Hydroxide Coated on $Ti_3C_2$ MXene for High-Performance Asymmetric Supercapacitor," *Applied Surface Science* 562 (2021): 150116.

22. Q. Wu, P. Li, Y. Wang, and F. Wu, "Construction and Electrochemical Energy Storage Performance of Free-standing Hexagonal $Ti_3C_2$ Film for Flexible Supercapacitor," *Applied Surface Science* 593 (2022): 153380.

23. M. A. K. Purbayanto, M. Chandel, D. Bury, et al., "Microwave-Assisted Hydrothermal Synthesis of Photocatalytic Truncated-Bipyramidal $TiO_2$/$Ti_3CN$ Heterostructures Derived From $Ti_3CN$ MXene," *Langmuir* 40, no. 41 (2024): 21547–21558.

24. L. Yu, W. Li, C. Wei, Q. Yang, Y. Shao, and J. Sun, "3D Printing of NiCoP/$Ti_3C_2$ MXene Architectures for Energy Storage Devices With High Areal and Volumetric Energy Density," *Nano-Micro Letters* 12, no. 1 (2020): 143.

25. M. Flygare and K. Svensson, "Influence of Crystallinity on the Electrical Conductivity of Individual Carbon Nanotubes," *Carbon Trends* 5 (2021): 100125.

26. M. N. Mustafa and Y. Sulaiman, "Optimization of Titanium Dioxide Decorated by Graphene Quantum Dot as a Light Scatterer for Enhanced Dye-Sensitized Solar Cell Performance," *Journal of Electroanalytical Chemistry* 876 (2020): 114516.

27. S. Nie, C. Zhang, C. Peng, D. Wang, D. Ding, and Q. He, "Study of the Synergistic Effect of Nanoporous Nickel Phosphates on Novel Intumescent Flame Retardant Polypropylene Composites," *Journal of Spectroscopy* 2015 (2015): 1–7.

28. H. Su, M. Xu, S. Zhou, et al., "Belt-Like Cobalt Phosphate Tetrahydrate as the Non-Noble Metal Catalyst With Enhanced Catalytic Reduction Activity," *ChemistrySelect* 3, no. 24 (2018): 6924–6934.

29. J. Chen, X. Yuan, F. Lyu, et al., "Integrating MXene Nanosheets With Cobalt-Tipped Carbon Nanotubes for an Efficient Oxygen Reduction Reaction," *Journal of Materials Chemistry A* 7, no. 3 (2019): 1281–1286.

30. M. N. Mustafa, S. Shafie, Z. Zainal, and Y. Sulaiman, "A Novel poly (3,4-ethylenedioxythiophene)-graphene Oxide/Titanium Dioxide Composites Counter Electrode for Dye-Sensitized Solar Cell," *Journal of Nanomaterials* 2017 (2017): 1–9.

31. M. N. Mustafa, S. Shafie, Z. Zainal, and Y. Sulaiman, "Poly(3,4-ethylenedioxythiophene) Doped With Various Carbon-Based Materials as Counter Electrodes for Dye Sensitized Solar Cells," *Materials & Design* 136 (2017): 249–257.

32. T. Parker, D. Zhang, D. Bugallo, et al., "Fourier-Transform Infrared Spectral Library of MXenes," *Chemistry of Materials* 36, no. 17 (2024): 8437–8446.

33. M. H. M. Facure, L. A. Mercante, Y. Gogotsi, and D. S. Correa, "ZnO–$Co_3O_4$ Nanofibers/MXene Composite With Peroxidase-Like Activity for Ascorbic Acid Detection," *ACS Applied Nano Materials* 8, no. 9 (2025): 4291–4299.

34. M. Liu, Y. Zhuo, A. Sarycheva, et al., "Deformation of and Interfacial Stress Transfer in $Ti_3C_2$ MXene-Polymer Composites," *ACS Applied Materials & Interfaces* 14, no. 8 (2022): 10681–10690.

35. R. Kang, Z. Zhang, L. Guo, et al., "Enhanced Thermal Conductivity of Epoxy Composites Filled With 2D Transition Metal Carbides (MXenes) With Ultralow Loading," *Scientific Reports* 9, no. 1 (2019): 9135.

36. A. Iqbal and N. M. Hamdan, "Investigation and Optimization of MXene Functionalized Mesoporous Titania Films as Efficient Photoelectrodes," *Materials* 14, no. 21 (2021): 6292.

37. B. A. Mahmoud, A. A. Mirghni, K. O. Oyedotun, D. Momodu, O. Fasakin, and N. Manyala, "Synthesis of Cobalt Phosphate-Graphene Foam Material via Co-Precipitation Approach for a Positive Electrode of an Asymmetric Supercapacitors Device," *Journal of Alloys and Compounds* 818 (2019): 153332.

38. W. Yan, D. Wang, and G. G. Botte, "Nickel and Cobalt Bimetallic Hydroxide Catalysts for Urea Electro-Oxidation," *Electrochimica Acta* 61 (2012): 25–30.

39. E. Pollack, Q. Zhou, E. Loni, et al., "Raman Spectroscopy of 2D $MoS_2$ on $Ti_3C_2$ MXene: The Substrate Effect," *Nanoscale Advances* 7, no. 11 (2025): 3456–3461.

40. R. Li, C. Liu, P. Tang, et al., "NiCoP Nanowire Arrays Embedded in 3D Integrated N-Doped Carbon Network for Enhanced Electrochemical Oxygen Evolution," *Vacuum* 192 (2021): 110395.

41. W. Yang, B. Huang, L. Li, et al., "Covalently Sandwiching MXene by Conjugated Microporous Polymers With Excellent Stability for Supercapacitors," *Small Methods* 4 (2020): 2000434.

42. A. Tanvir, P. Sobolčiak, A. Popelka, et al., "Electrically Conductive, Transparent Polymeric Nanocomposites Modified by 2D $Ti_3C_2T_x$ (MXene)," *Polymers* 11, no. 8 (2019): 1272.

43. A. Liu, M. Gao, X. Ren, et al., "A Two-Dimensional Ru@MXene Catalyst for Highly Selective Ambient Electrocatalytic Nitrogen Reduction," *Nanoscale* 12, no. 20 (2020): 10933–10938.

44. Y. Zhu, Q. Zong, Q. Zhang, H. Yang, Q. Wang, and H. Wang, "Three-Dimensional Core-Shell NiCoP@NiCop Array on Carbon Cloth for High Performance Flexible Asymmetric Supercapacitor," *Electrochimica Acta* 299 (2019): 441–450.

45. S. K. Babu, J. J. D. Raj, T. Vijayakumar, and B. Gunasekaran, "Experimental and DFT Studies on Spinel $NiMn_2O_4$ Flower Derived From Bimetallic MOF as an Efficient Electrode for Next-Generation Supercapacitor," *Colloids and Surfaces, A: Physicochemical and Engineering Aspects* 655 (2022): 130244.

46. J. Fan, K. Wu, A. Chen, M. Wang, X. Xie, and J. Fan, "Fingerprint-Like NiCoP Electrode Material With Rapid Charging/Discharging Performance Under Large Current Density," *Journal of Alloys and Compounds* 902 (2022): 163866.

47. D. Zeng, W. J. Ong, Y. Chen, et al., "$Co_2P$ Nanorods as an Efficient Cocatalyst Decorated Porous g-$C_3N_4$ Nanosheets for Photocatalytic Hydrogen Production Under Visible Light Irradiation," *Particle & Particle Systems Characterization* 35, no. 1 (2018): 1700251.

48. Z. Zou, Q. Wang, J. Yan, et al., "Versatile Interfacial Self-Assembly of $Ti_3C_2T_x$ MXene Based Composites With Enhanced Kinetics for Superior Lithium and Sodium Storage," *ACS Nano* 15, no. 7 (2021): 12140–12150.

49. L. Yue, D. Jia, J. Tang, et al., "Improving the Rate Capability of Ultrathin NiCo-LDH Nanoflakes and FeOOH Nanosheets on Surface Electrochemically Modified Graphite Fibers for Flexible Asymmetric Supercapacitors," *Journal of Colloid and Interface Science* 560 (2020): 237–246.

50. M. N. Mustafa, S. Shafie, M. H. Wahid, and Y. Sulaiman, "Optimization of Power Conversion Efficiency of Polyvinyl-Alcohol/Titanium Dioxide as Light Scattering Layer in DSSC Using Response Surface Methodology/Central Composite Design," *Results in Physics* 15 (2019): 102559.

51. M. N. Mustafa, S. Shafie, M. H. Wahid, and Y. Sulaiman, "Optimization of Power Conversion Efficiency of Polyvinyl-Alcohol/Titanium Dioxide Compact Layer Using Response Surface Methodology/Central Composite Design," *Solar Energy* 183 (2019): 689–696.

52. D. Chu, X. Qu, S. Zhang, et al., "Polyoxometalate/MXene Hybrid Film With a 3D Porous Structure for High-Performance Electrochromic Supercapacitors," *Materials Today Chemistry* 30 (2023): 101561.

53. J. Kim, K. H. Lee, S. Lee, et al., "Minimized Optical Scattering of MXene-Derived 2D $V_2O_5$ Nanosheet-Based Electrochromic Device With High Multicolor Contrast and Accuracy," *Chemical Engineering Journal* 453 (2023): 139973.

54. X. Qu, S. Zhou, Z. Wang, et al., "Polyoxometalates/MXenes Hybrid Film With Synchronous Enhancement of Electron and Proton Transport Efficiency for Smart Electrochromic Supercapacitors," *Materials Today Chemistry* 50 (2025): 103124.

55. V.-T. Nguyen, B. K. Min, S. K. Kim, Y. Yi, and C.-G. Choi, "A Flexible and High-Performance Electrochromic Smart Window Produced by $WO_3/Ti_3C_2T_x$ MXene Hybrids," *Journal of Materials Chemistry C* 9, no. 9 (2021): 3183–3192.

56. M. N. Mustafa, M. A. A. Mohd Abdah, N. Mohamad Saidi, et al., "High-Performance Electrochromic Supercapacitor With Bimetallic Phosphate and Vanadium Carbide MXene," *Journal of Power Sources* 595 (2024): 234079.

57. W. Wu, C. Zhao, D. Niu, et al., "Ultrathin N-Doped $Ti_3C_2$-MXene Decorated With $NiCo_2S_4$ Nanosheets as Advanced Electrodes for Supercapacitors," *Applied Surface Science* 539 (2021): 148272.

58. M. A. A. M. Abdah, J. Cherusseri, N. A. Dzulkarnain, et al., "Facile Synthesis of Microwave-Etched $Ti_3C_2$ MXene/Activated Carbon Hybrid for Lithium-Ion Battery Anode," *Journal of Electroanalytical Chemistry* 928 (2023): 117050.

59. N. A. Jalil, M. A. A. Mohd Abdah, N. H. N. Azman, and Y. Sulaiman, "Polyaniline and Manganese Oxide Decorated on Carbon Nanofibers as a Superior Electrode Material for Supercapacitor," *Journal of Electroanalytical Chemistry* 867 (2020): 114188.

60. M. A. A. Mohd Abdah, N. A. Zubair, N. H. N. Azman, and Y. Sulaiman, "Fabrication of PEDOT Coated PVA-GO Nanofiber for Supercapacitor," *Materials Chemistry and Physics* 192 (2017): 161–169.

61. S. Li, Q. Zhang, L. Liu, et al., "Ultra-Stable Sandwich Shaped Flexible MXene/CNT@Ni Films for High Performance Supercapacitor," *Journal of Alloys and Compounds* 941 (2023): 168963.

62. I. Ashraf, S. Ahmad, D. Dastan, and M. Iqbal, "Ni-Doped $CeO_2$ Decorated Delaminated Layered Titanium Carbonitride (d-$Ti_3CN$) MXene for Potential Applications in Symmetric Supercapacitors," *Journal of Alloys and Compounds* 952 (2023): 170043.

63. M. Cai, X. Wei, H. Huang, et al., "Nitrogen-Doped $Ti_3C_2T_x$ MXene Prepared by Thermal Decomposition of Ammonium Salts and Its Application in Flexible Quasi-Solid-State Supercapacitor," *Chemical Engineering Journal* 458 (2023): 141338.

64. Y. Wang, X. Wang, X. Li, et al., "Intercalating Ultrathin $MoO_3$ Nanobelts into MXene Film With Ultrahigh Volumetric Capacitance and Excellent Deformation for High-Energy-DensITy Devices," *Nano-Micro Letters* 12, no. 1 (2020): 115.

65. J. Yan, C. E. Ren, K. Maleski, et al., "Flexible MXene/Graphene Films for Ultrafast Supercapacitors With Outstanding Volumetric Capacitance," in *MXenes* (Jenny Stanford Publishing, 2023), 583–608.

66. W. Liu, Z. Wang, Y. Su, Q. Li, Z. Zhao, and F. Geng, "Molecularly Stacking Manganese Dioxide/Titanium Carbide Sheets to Produce Highly Flexible and Conductive Film Electrodes With Improved Pseudocapacitive Performances," *Advanced Energy Materials* 7, no. 22 (2017): 1602834.

67. M. A. A. Mohd Abdah, N. S. Mohd Razali, P. T. Lim, S. Kulandaivalu, and Y. Sulaiman, "One-Step Potentiostatic Electrodeposition of Polypyrrole/Graphene Oxide/Multi-Walled Carbon Nanotubes Ternary Nanocomposite for Supercapacitor," *Materials Chemistry and Physics* 219 (2018): 120–128.

68. M. A. A. Mohd Abdah, N. Abdul Rahman, and Y. Sulaiman, "Enhancement of Electrochemical Performance Based on Symmetrical Poly-(3,4-ethylenedioxythiophene) Coated Polyvinyl Alcohol/Graphene Oxide/Manganese Oxide Microfiber for Supercapacitor," *Electrochimica Acta* 259 (2018): 466–473.